npj | climate and atmospheric science

Article

Published in partnership with CECCR at King Abdulaziz University

https://doi.org/10.1038/s41612-024-00616-2

Skillful prediction of length of day one year ahead in multiple decadal prediction systems

Hyunsuk Yoon [1], Jung Choi [1] ✉, Seok-Woo Son [1] ✉ & Adam A. Scaife [2,3]

Despite a small amplitude, Length of Day (LOD) change, which varies from one year to another due to changes in Atmospheric Angular Momentum (AAM), determines the accuracy of Global Positioning System (GPS) time calculation. In this study, we examine the prediction skill of LOD and AAM in nine decadal prediction systems archived for the Decadal Climate Prediction Project. A persistence and rebound in LOD prediction skill at one year or longer lead time is found in most models. A poleward propagation of AAM anomaly via wave-mean flow interaction is also qualitatively well reproduced. This long-lead prediction of LOD and AAM is attributed to reliable predictions of the El Niño–Southern Oscillation (ENSO) and the Quasi-Biennial Oscillation (QBO), the former being more systematically related than the latter. This result indicates that the improved ENSO prediction and atmospheric wave-mean flow interaction may lead to better prediction of LOD, AAM and related extratropical climate in the decadal prediction systems.

Length of Day (LOD), or the Earth's rotation rate, does not remain constant but varies in time at the scale of up to a few milliseconds[1]. Its variation on decadal timescales or longer mainly arises from tidal torques by celestial bodies [2,3] or interaction between the Earth's core and mantle[4–6]. Meanwhile, its variation on interannual or shorter time scales is often related to the solid Earth's interaction with the atmosphere, i.e., the transfer of angular momentum between the Earth and the atmosphere[1,4,7–9]. Considering the Earth system as an isolated system, changes in Atmospheric Angular Momentum (AAM) are compensated by changes in the angular momentum of the solid Earth, which leads to changes in the Earth's rotation rate and LOD.

Among various atmospheric phenomena, El Niño–Southern Oscillation (ENSO) and Quasi-Biennial Oscillation (QBO) are known to play an important role in the interannual variation of AAM and LOD[1]. It has been known that ENSO well explains the LOD variation on interannual or shorter time scales; for instance, one study[10] showed that ENSO has a correlation of 0.58, −0.48, and 0.46 with annual, semi-annual, and short-term trend of LOD variation, respectively. Strong El Niño events can increase the LOD by about 750 μs. When accumulated, it can result in a net decrease in the universal time (UT1) by 0.1 s, which is three times greater than its seasonal variation (~±30 ms)[11]. The LOD shows a delayed response to ENSO by one to three months[12–15], as it takes a few months for the large-scale atmospheric environment to respond to ENSO-related SST anomalies[15]. Strong ENSO events also show high coherence with LOD on interannual time scale[16]. The El Niño typically accompanies weakening of tropical easterlies and strengthening of subtropical jet via thermal wind balance, which leads to an increase in AAM and LOD[15,17–19]. It is noted that strengthening or weakening of jet induced by El Niño- or La Niña-like changes in sea surface temperature, respectively, are also associated with long-term changes or climate shifts in AAM[20]. The QBO is also closely associated with LOD as manifested by quasi-biennially oscillating component within LOD[13,21]. The linear combination of these two climate variabilities can explain a majority ($r = 0.75$) of interannual variation of LOD[13]. Between them, ENSO more significantly contributes to LOD variation, explaining twice as much as QBO. However, a significant coherence between the linearly combined ENSO-QBO signals and LOD at biennial periods indicates a non-negligible contribution of QBO to LOD[13].

A recent study has shown that LOD can be predictable at long lead times. Using the UK Met Office Hadley Centre Global Environmental Model of the atmosphere and ocean, Scaife et al.[22] showed that the prediction skill of LOD remains significantly high for over a year with a skill rebound at about a year after model initialization. Such a prolonged persistence of LOD prediction skill was attributed to the long residence and propagation of AAM anomaly from the tropics to the extratropics via wave-mean flow interaction. Their result indicates that LOD and AAM may potentially be a powerful predictor for long-range prediction of extratropical

[1]School of Earth and Environmental Sciences, Seoul National University, Seoul, South Korea. [2]Met Office Hadley Centre, Exeter, UK. [3]Faculty of Environment, Science and Economy, University of Exeter, Exeter, UK. ✉e-mail: jungchoi@snu.ac.kr; seokwooson@snu.ac.kr

climate. However, as they used a single model, whether such behavior of LOD prediction skill can be generalized to other models is not yet examined.

In this study, we extend the previous study[22] by investigating (1) whether non-monotonic LOD and AAM prediction skills, with significant skills at lead time longer than a year, are commonly found in multiple decadal prediction systems and (2) whether LOD prediction skill is related to tropical climate variabilities such as ENSO and QBO.

Results

LOD and AAM prediction skills

The time series of the observed LOD anomaly is shown in Fig. 1a (black line). The amplitude of LOD anomaly is locked to the seasonal cycle. It shows a larger variability in late winter ($\sigma = 0.24$ ms in January–March; JFM) than in other seasons (~0.17 ms) (Supplementary Table 1). It also exhibits an asymmetry in the amplitude between the positive and negative events, the positive LOD anomaly being larger than the negative one. As in the amplitude of LOD anomaly, the asymmetry (i.e., skewness of LOD anomaly) is also locked to the seasonal cycle, showing a larger amplitude in late winter (0.56 ± 0.19 in JFM) than in other seasons ($\sim 0.22 \pm 0.19$) (Supplementary Table 2). These features of LOD resemble the general characteristics of ENSO seasonality, with ENSO activity peaking in boreal winter.

The LOD anomalies from Japanese 55-year Reanalysis data (JRA-55) and the Coupled Model Intercomparison Project (CMIP) phase 6 decadal climate prediction project (CMIP6 DCPP) multi-model ensemble mean (hereafter MMM) prediction are also shown in red and blue, respectively, in Fig. 1a. JRA-55 well reproduces the observed time series of LOD anomaly ($r = 0.75$, $p < 0.05$). The overall variability of LOD anomaly ($\sigma = 0.14$ ms) is comparable to that of observation (0.19 ms) (Supplementary Table 1). Its seasonal cycle is also qualitatively reproduced ($\sigma = 0.19$ ms in JFM; ~0.12 ms in other seasons). This indicates that JRA-55 can be regarded as a reliable baseline for studying LOD and AAM. It has been known that LOD and AAM exhibit intraseasonal variability, such as the 30–90 day signal associated with the Madden–Julian Oscillation[8,23]. In MMM, however, such signal is filtered out by the ensemble mean, resulting in a smoothed time series with an underestimated amplitude compared to the observation. Although underestimated, MMM reasonably predicts the observed interannual variation of LOD anomaly months to a year ahead ($r = 0.47$, $p < 0.05$) and reproduces the seasonal locking of its variability ($\sigma = 0.13$ ms in JFM; ~0.06 ms in other seasons) (Supplementary Table 1). This result is consistent with ref. [22].

Figure 1b, c illustrates the AAM anomaly at each latitude and time from JRA-55 and MMM prediction, respectively. As LOD anomaly is proportional to global AAM (GAAM) anomaly (Eq. (3)), the time and place of zonal wind anomaly responsible for anomalous LOD can be deduced from these figures. In both JRA-55 and MMM prediction, positive AAM anomaly occurs in strong El Niño winters (e.g., 1982/83, 1997/98, 2015/16), while negative AAM anomaly occurs in strong La Niña winters (e.g., 1973/74, 1988/89, 1998/99, 1999/2000, 2007/08, 2010/11), consistent with the features of LOD anomaly as highlighted in Fig. 1a. This result suggests that AAM anomaly is triggered in the tropics, and propagates poleward to the extratropics (Fig. 1b). The poleward propagation has been explained by the zonal mean mass circulations in the subtropics[8] and the interaction between zonal flow and transient eddies in the extratropics[22,24–26], although the detailed mechanisms are not fully understood. In particular, it has been proposed that the stationary eddies and zonal mean mass circulations associated with tropical convection anomalies are partly responsible for the AAM propagation in the subtropical region[8]. In the context of linear wave dynamics, the critical latitude at which the equatorward-propagating transient eddies dissipate has also been proposed to play an important role.

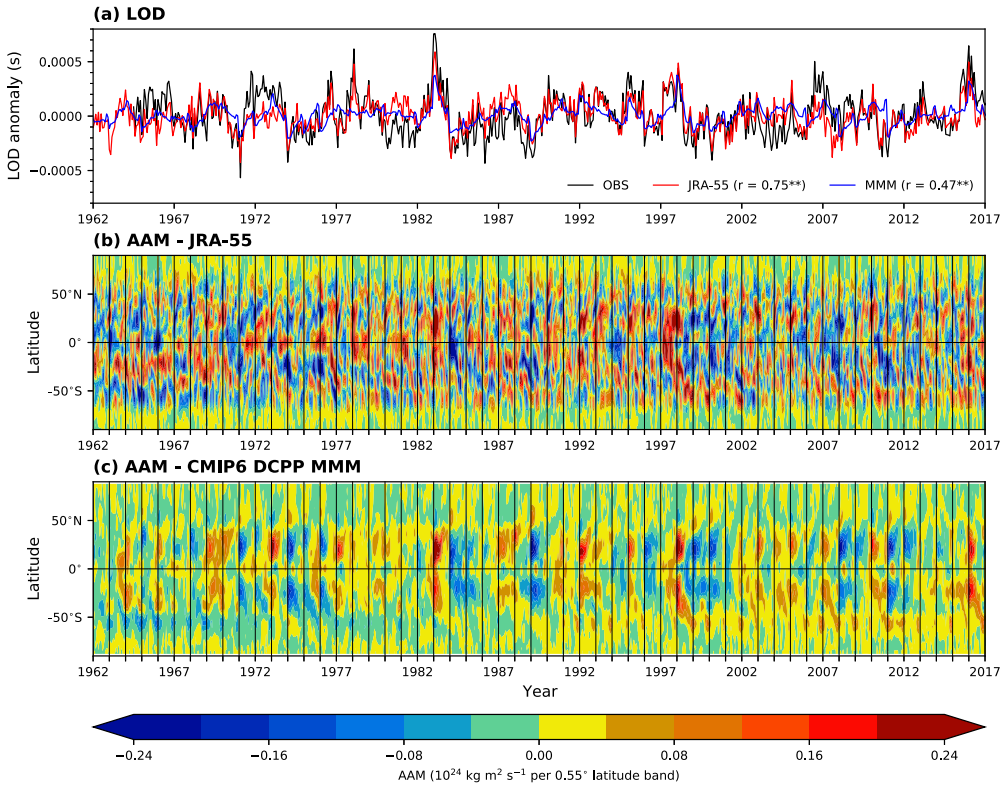

Fig. 1 | LOD and AAM anomalies in the observation, JRA-55, and CMIP6 DCPP MMM predictions. a Monthly LOD anomaly from the observation (black), JRA-55 (red) and 1-year predictions (1–12 lead months) of CMIP6 DCPP MMM starting from the first January (lead month = 1) since model initialization (blue). Numbers in parentheses represent each data's correlation with observation. Significant values at the 95% confidence level, based on the two-tailed Student's *t*-test, are indicated with double asterisks. **b** Latitude-time evolution of AAM anomalies from JRA-55. Vertical lines indicate January of each year. **c** Same as (**b**) but for 1-year predictions (1–12 lead months) of CMIP6 DCPP MMM starting from the first January (lead month = 1) since model initialization.

As transient waves break around the critical latitude, the zonal wind weakens and the critical latitude shifts poleward. This can lead to a poleward propagation of the AAM anomaly[22,25,26].

Regardless of the detailed dynamical mechanism(s) of AAM changes, MMM qualitatively well predicts the observed fluctuation and propagation of AAM anomaly months to a year ahead (Fig. 1c). The symmetric poleward-migrating behavior of AAM anomaly about the equator is also qualitatively reproduced in MMM prediction. However, the variability of AAM anomaly in MMM (peak of 8.9×10^{22} kg m^2 s^{-1} at 21°N) is significantly smaller than that of JRA-55 (peak of 1.7×10^{23} kg m^2 s^{-1} at 24°N) at the 95% confidence level. This can be simply attributed to averaging effect of multiple model ensembles. Individual members reproduce the latitudinal distribution of AAM variability both qualitatively (spatial correlation $r \geq 0.9$ when interpolated to reanalysis grid) and quantitatively (peak of $1.4–2.2 \times 10^{23}$ kg m^2 s^{-1} at 20–40°N/S) (not shown).

The model prediction skills of LOD and AAM are quantitatively summarized in Fig. 2 in terms of anomaly correlation coefficient (ACC; Eq. (6)). The LOD prediction skill decreases with lead times and rebounds at ~1 year after initialization in most models and MMM (Fig. 2a). This is again consistent with the previous study[22] who reported the re-emergence of LOD prediction skill in the second winter (peak at 15 lead month, which corresponds to 14 lead month in Fig. 2a) from a single decadal prediction system. Thus, Fig. 2a extends their results[22] by showing that such non-monotonic behavior of LOD prediction skill is robustly found in multiple decadal prediction systems. Note that MMM prediction surpasses individual models at 12–15 lead months. This superior performance of MMM might result from a large ensemble size and/or a multi-model ensemble effect, as in other climate property predictions[27].

To identify where the re-emergence of LOD prediction skill comes from, the prediction skill of AAM is illustrated for each latitude and lead time in Fig. 2b. A poleward propagation of statistically significant AAM prediction skill by MMM is observed along the latitudes where AAM anomaly propagates (50°S–50°N). This is evident up to 18 months after initialization. The AAM prediction skill also shows a sign of rebound at 12–15 lead months, which is consistent with Fig. 2a. When the AAM is detrended, the AAM prediction skill at ~60°S about a year later disappears (Supplementary Fig. 1). This suggests that a rebound of AAM prediction skill in the Southern Hemisphere (SH) extratropics may have resulted from the long-term strengthening of the SH polar jet due to the ozone hole especially in the austral summer. Nevertheless, as the AAM is associated with extratropical climate components such as the mid-latitude jet[22], Fig. 2 implies a potential of LOD and AAM as useful predictors for mid-latitude climate from months to over a year.

LOD prediction skills and tropical climate variabilities

As discussed earlier, two tropical climate variabilities, i.e., ENSO and QBO, significantly affect the year-to-year changes in LOD anomaly[13]. To quantify their effect in long-term predictions, the LOD anomaly is reconstructed by performing the multiple regression of the ENSO and QBO indices from observation (Eq. (4)). As shown in Fig. 3a, the reconstructed LOD anomaly accounts for one-third of the observed total variability in LOD anomaly with a correlation coefficient of 0.55 ($p < 0.05$, red solid line). The ENSO-based reconstruction also explains the observed LOD anomaly variability to similar extent ($r = 0.46$, $p < 0.05$, red dashed line). It confirms that the interannual variation of LOD anomaly is closely associated with ENSO and QBO, the former being more important than the latter. When multiple regression analysis is conducted using standardized LOD, ENSO and QBO indices, the regression coefficient for ENSO (0.47 ± 0.033) is found to be about 1.6 times as large as that for QBO (0.30 ± 0.034). This is qualitatively consistent with the previous study[13] who showed that ENSO and QBO can well explain the interannual variation of LOD anomaly, with ENSO contributing almost twice as much as QBO in terms of interannual standard deviation.

When the reconstructed LOD index in MMM is generated using regression coefficients from observation (Eqs. (4) and (5)) assuming perfect prognostic[28], it also closely follows the interannual variation of LOD anomaly in MMM but to a greater extent compared to the observation (Fig. 3b). Both ENSO&QBO-based and ENSO-based indices show significant ($p < 0.05$) correlations with LOD anomaly ($r = 0.89$ and $r = 0.88$, respectively). Their difference is negligible, indicating a strong relationship between LOD and ENSO, with a minimal influence of QBO. Although not shown, the results are almost identical when using model output statistics or regression coefficients from the MMM prediction. This result suggests that a minor but non-negligible contribution of the QBO to the LOD variation is not captured in the model predictions.

The relationship between LOD and tropical climate variabilities is further illustrated in Fig. 4 in terms of model prediction skill. Figure 4a shows that significant LOD prediction skill is observed in the first 5–10 months and re-emerges in 12–15 lead months for most models. The majority of the models also show a significant ENSO prediction skill for the first 13–19 months (Fig. 4b). This is consistent with Choi and Son[27] who found significant ENSO prediction skill up to 25–27 lead months by MMM of CMIP phase 5 and 6 models. The rapid decrease and the absence of

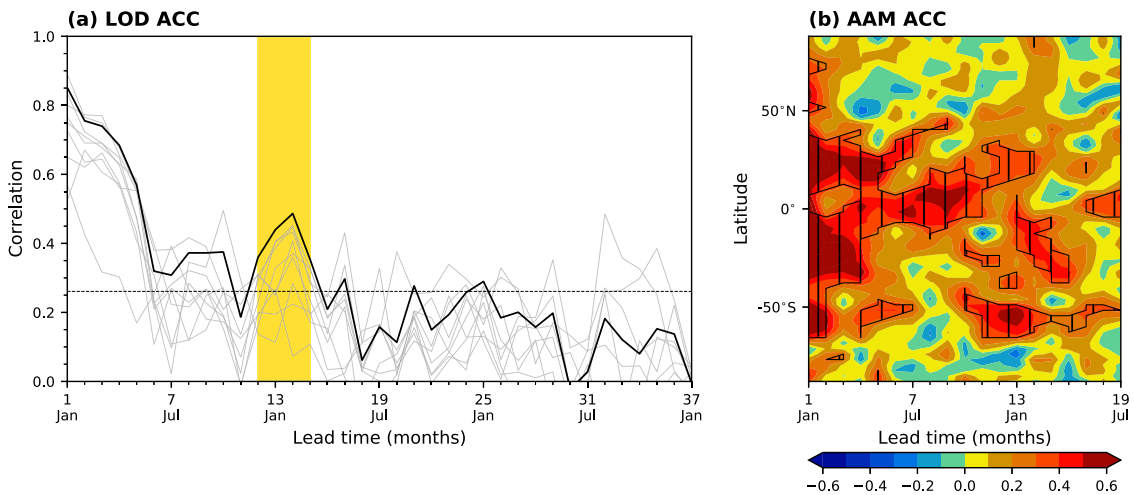

Fig. 2 | LOD and AAM prediction skills of CMIP6 DCPP models. a LOD prediction skill of individual CMIP6 DCPP models (gray lines) and MMM (thick black line). The black dashed line indicates the statistically significant skill at the 95% confidence level based on the two-tailed Student's *t*-test. Lead times when LOD prediction skill of MMM rebounds (12–15 months) are shaded with yellow. **b** AAM prediction skill of CMIP6 DCPP MMM as a function of latitude and lead time. Statistically significant values at the 95% confidence level, based on the two-tailed Student's *t*-test, are hatched. In (**a**, **b**), lead time 1 indicates the first January since model initialization.

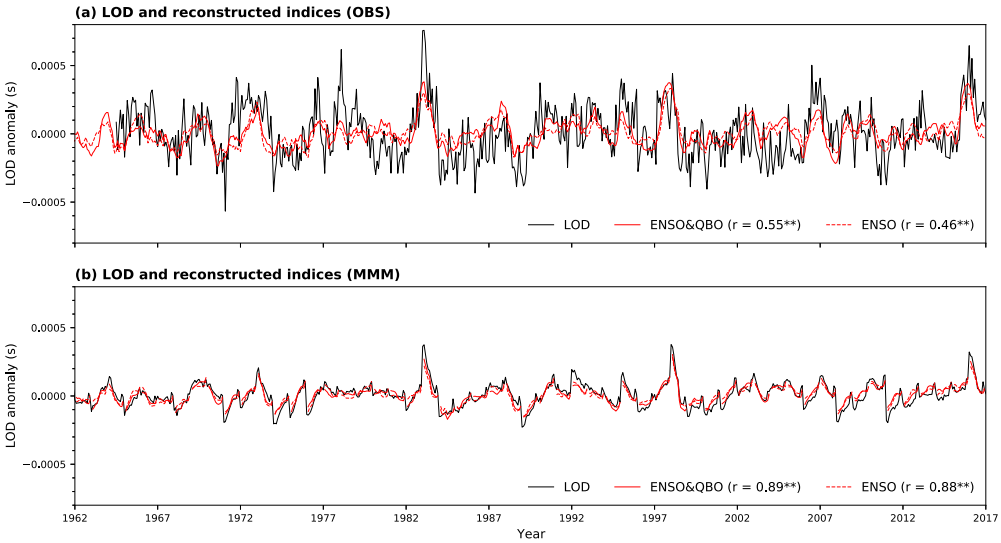

Fig. 3 | Time series of LOD and reconstructed LOD indices. a Time series of LOD anomaly from the observation (black line), ENSO&QBO-based reconstruction (red solid line) and ENSO-based reconstruction (red dashed line). The ENSO&QBO-based reconstruction is constructed by a linear combination of lagged Niño3 index from ERSSTv5 and 30-hPa equatorial zonal wind index from JRA-55 that best explains the observed LOD variation. The ENSO-based reconstruction is similarly constructed but using Niño3 index only. Numbers in parentheses represent the correlation between the LOD anomaly and each index. Significant values at the 95% confidence level, based on the two-tailed Student's *t*-test, are indicated with double asterisks. **b** Same as (**a**) but for LOD anomaly and reconstructed LOD indices from MMM.

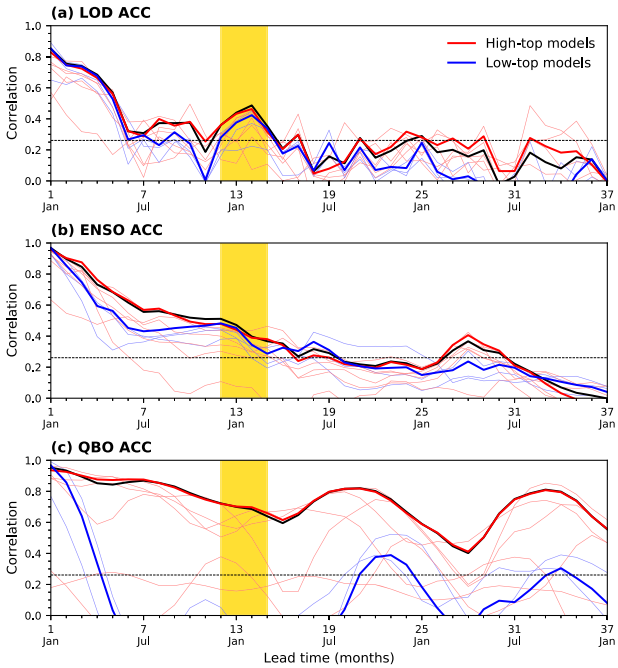

Fig. 4 | Prediction skills of LOD, ENSO and QBO. a LOD prediction skill of CMIP6 DCPP models, same as Fig. 2a but separately showing high-top (red) and low-top models (blue). Result for MMM (black) is identical to that in Fig. 2a, and shown here as a reference. **b**, **c** Same as (**a**) but for ENSO and QBO prediction skills, respectively.

"spring barrier" in ENSO prediction skill in Fig. 4b compared to their results[27] may in part be attributable to differences in models considered or analysis periods. Meanwhile, the behavior of QBO prediction skill shows a strong model dependency (Fig. 4c). Some models, such as HadGEM3-GC31-MM and MPI-ESM1-2-HR, predict QBO with lead times up to two years or longer. This is qualitatively consistent with refs. [29,30], who have reported high prediction skill ($r > 0.7$) at 12 lead months in similar decadal prediction models; quantitative differences exist presumably due to different version of models analyzed. On the other hand, some models, such as NorCPM1, fail to predict QBO even at short lead times. This may be associated with low model top and the consequent limitation in fully representing stratospheric processes[31]. It is noticeable that the QBO prediction skill tends to decrease in most models during the boreal late spring and early summer, especially in the high-top models (see 16 and 28 lead months in Fig. 4c). Although unconfirmed, this may be related to the fact that QBO phase transitions, which are less predictable than the westerly or easterly QBO phases, occur more frequently in similar seasons[32,33].

To clarify the impact of model top height on the models' prediction skills, Fig. 4a re-examines individual models' LOD prediction skills by separately considering high-top and low-top models. Individual models' ENSO and QBO prediction skills are also illustrated in Fig. 4b, c. As shown in Fig. 4a, high-top models have slightly better LOD prediction skills than low-top models. This may be partly related with model prediction skill of QBO. High-top models show significantly higher QBO prediction skill than low-top models at lead times of 5–19 months (Fig. 4c). For ENSO prediction, although statistically insignificant, high-top models also outperform low-top models at relatively short lead times of up to 10 months (Fig. 4b). However, both model groups show similar ENSO prediction skill at 12–15 lead months. This may explain the minor difference in LOD prediction skill between high- and low-top models at the lead times of skill re-emergence (Fig. 4a). This result indicates that LOD prediction skill is more strongly associated with ENSO prediction skill than QBO prediction skill.

To address an inter-model spread of LOD prediction skill and their relationships with the ENSO and QBO prediction skills, the LOD prediction skill of ensemble-mean and individual models are compared with those using the reconstructed LOD indices in Fig. 5. Here the reconstructed LOD indices, $LOD_{E\&Q}$ and LOD_{E}, are defined by applying Eqs. (4) and (5), respectively, to individual ensemble members. The inter-model spread of LOD prediction skills is largely explained by the prediction skills of the $LOD_{E\&Q}$ with $r = 0.88$ ($p < 0.05$) (Fig. 5a). When all 80 ensemble members are considered as independent samples, LOD prediction skills are also positively correlated with the $LOD_{E\&Q}$ prediction skills with $r = 0.81$ ($p < 0.05$) (Fig. 5a). It indicates that the ensemble members with higher ENSO and QBO prediction skills tend to have higher LOD prediction skills. Quantitatively similar results are found when only ENSO index is taken into account (Fig. 5b). Although not shown, when directly comparing ENSO and LOD prediction skills, the spread of ensemble-mean and individual

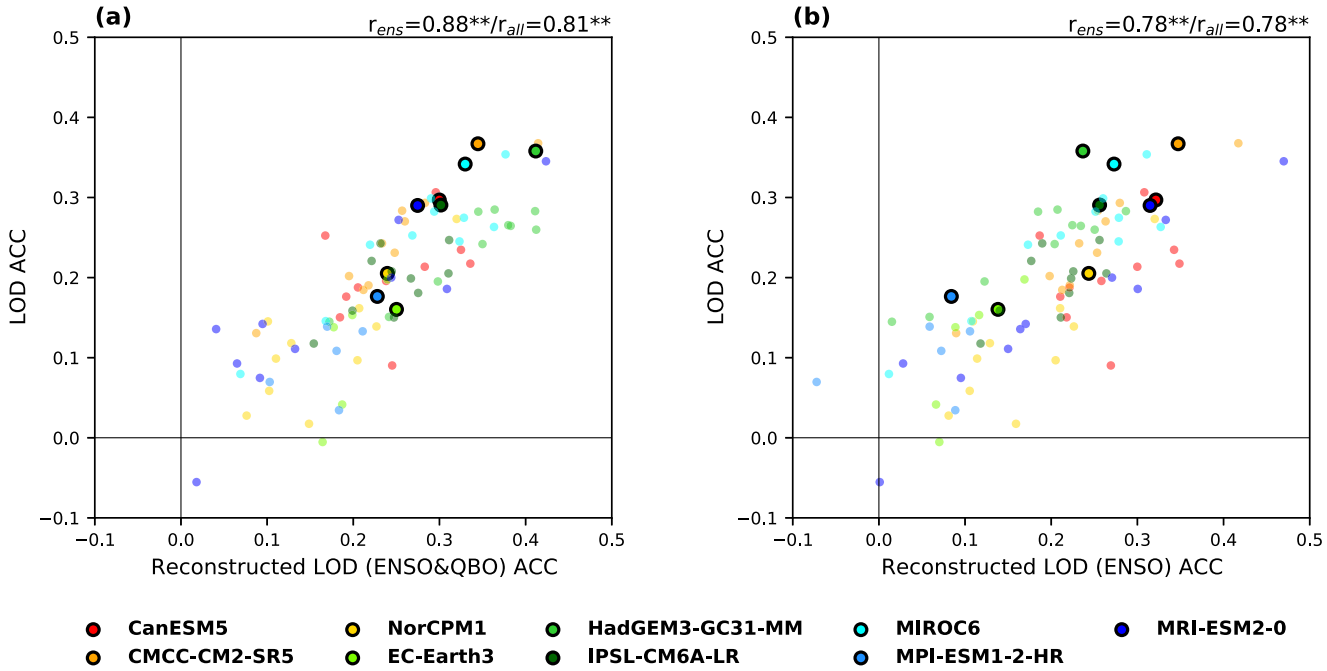

Fig. 5 | Relationship of prediction skills between LOD and reconstructed LOD indices. a Scatter plot of LOD versus ENSO&QBO-based LOD reconstruction prediction skills averaged over 12–15 lead months (December–March). For each model, the ensemble mean is shown in bold marker whereas individual members are shown in dim markers. Numbers at the upper right corner represent the correlation of prediction skills between LOD and reconstructed LOD indices for ensemble-mean predictions (first number; $n = 9$) and all individual predictions (second number; $n = 80$). Significant values at the 95% confidence level, based on the two-tailed Student's t-test, are noted with double asterisks. **b** Same as (**a**) but for ENSO-based LOD reconstruction.

members show correlation coefficients of 0.58 ($p > 0.05$) and 0.61 ($p < 0.05$), respectively; no significant correlations ($r = -0.16$ and $r = 0.11$, respectively) are found when just QBO and LOD prediction skills are compared. These results again suggest that LOD prediction skill is more sensitive to ENSO prediction skill than QBO prediction skill in decadal prediction systems.

Discussion

As LOD is an Earth rotation parameter whose precise measurement is vital for GPS applications, the mechanisms and relevant factors of its subtle yet important variation have long been studied. A recent study by ref. [22] showed that LOD is predictable more than a year ahead. However, although the interannual LOD variation is known to be closely associated with AAM variation mainly driven by ENSO and QBO, the relationship between LOD prediction skill and ENSO/QBO prediction skill has not been reported thus far. In this regard, the present study investigates LOD and AAM prediction skills in the multiple decadal prediction systems and their potential linkage to ENSO and QBO prediction skills.

The nine decadal prediction systems, that have participated in the CMIP6 DCPP, reasonably reproduce the observed fluctuation and poleward propagation of LOD and AAM anomalies. The long persistence and rebound of prediction skills of LOD and AAM anomalies at about a year later are found in most models and MMM, thus generalizing the results of ref. [22]. It is further found that LOD prediction skill is significantly correlated with ENSO and QBO prediction skills. In particular, ENSO prediction skill is highly correlated with LOD prediction skill ($r = 0.78$, $p < 0.05$; Fig. 5b), explaining nearly 60% of inter-model differences in LOD prediction skill. QBO prediction skill also contributes to a slight increase in correlation between LOD and reconstructed LOD prediction skills (Fig. 5a); however, its contribution to inter-model spreads in LOD prediction skill is marginal (less than 3.2%; not shown). Although the LOD variation explained by the QBO is not negligible in the observation (Fig. 3a; see also ref. [13]), the LOD prediction skill is only weakly influenced by the QBO in climate model predictions, as shown in Figs. 4, 5. It is yet unclear why the QBO-LOD relationship is underestimated in the models, but it may imply that stratosphere-troposphere coupling processes should be improved in the climate models.

The present study suggests that decadal prediction systems can have more accurate prediction of LOD when their predictions for ENSO, QBO, and their teleconnections are improved. Thus, whether model can reproduce the linkage between LOD and tropical climate variabilities is important for a skillful and reliable prediction of LOD and AAM. Since LOD and AAM are associated with mid-latitude climate components[22], this may also lead to improved long-range prediction of extratropical climate. Further investigation of the dynamics of poleward AAM propagation, which is not yet completely resolved, will help us to better understand how AAM and LOD signals influence the mid-latitude climate components and their prediction.

Methods

Length of day

In this study, we used the Earth Orientation Parameters 14 Combined 04 (EOP 14 C04) dataset, provided by the International Earth Rotation and Reference System Service (IERS). This dataset provides the daily LOD observation data from 1962 to now with one-month latency measured by techniques including Very Long Baseline Interferometry (VLBI), Satellite Laser Ranging (SLR), and Global Navigation Satellite Systems (GNSS) (https://www.iers.org/IERS/EN/DataProducts/EarthOrientationData/eop.html). The daily LOD data from 1960 to 2019 (60 years) is converted to monthly data, and LOD anomaly is calculated by removing its seasonal cycle (1960–2019) and 5-year running mean as in ref. [22].

For reanalysis and model data, global AAM (GAAM) is computed as shown in Eqs. (1), (2), and then its anomaly is converted to LOD anomaly using the approximation shown in Eq. (3).

$$\begin{aligned} \mathrm{AAM} &= \int_a^{\infty}\int_0^{2\pi}\rho\left(\Omega r\cos\varphi + U\right)r^3\cos^2\varphi\,\mathrm{d}\lambda\mathrm{d}r \\ &\cong \sum_0^{p_s}\sum_0^{2\pi}\left(\Omega a\cos\varphi + U\right)a^3\cos^2\varphi\Delta\lambda\frac{\Delta p}{g} \end{aligned} \quad (1)$$

Table 1 | List of CMIP6 DCPP models used in this study

Group	Model name	Initialized month	Initialized years	Ensemble size	Model top	Number of latitude grid points
High-top	EC-Earth3	November	1960–2016	5	0.01 hPa	256
	HadGEM3-GC31-MM	November	1960–2016	10	85 km	325
	IPSL-CM6A-LR	January	1961–2017	10	80 km	143
	MIROC6	November	1960–2016	10	0.004 hPa	128
	MPI-ESM1-2-HR	November	1960–2016	5	0.01 hPa	192
	MRI-ESM2-0	November	1960–2016	10	0.01 hPa	160
Low-top	CanESM5	January	1961–2017	10	1 hPa	64
	CMCC-CM2-SR5	November	1960–2016	10	~2 hPa	192
	NorCPM1	October	1960–2016	10	~2 hPa	96

Models with top height above 1-hPa level are considered as high-top models, whereas the remaining models are considered as low-top models.

$$\mathrm{GAAM} = \int_{-\pi/2}^{\pi/2} \mathrm{AAM}\, \mathrm{d}\varphi \cong \sum_{-\pi/2}^{\pi/2} \mathrm{AAM}\, \Delta\varphi \tag{2}$$

$$\tau - \tau_\mathrm{r} \cong \frac{\Delta\mathrm{GAAM} \times \tau_\mathrm{r}^2}{2\pi I} \tag{3}$$

where ρ is the atmospheric density, Ω is the mean angular velocity of the Earth ($7.292116 \times 10^{-5}\ \mathrm{s}^{-1}$), U is the zonal wind, g is the mean gravitational acceleration ($9.80665\ \mathrm{m\ s}^{-2}$), r is the radial distance from the Earth's center, a is the mean radius of the Earth (6371.229 km), φ is latitude, λ is longitude, p is atmospheric pressure, and p_s is the pressure of the bottommost layer. In Eq. (3), ΔGAAM is the fluctuation of GAAM in time, τ_r is the reference LOD (86400 s), and τ is the observed LOD from the EOP 14 C04 dataset. I is a constant moment of inertia of the solid Earth ($8 \times 10^{37}\ \mathrm{kg\ m}^2$).

In Eq. (1), AAM is defined as the absolute angular momentum of the atmosphere integrated in zonal and vertical directions. It is thus defined at each time and latitude. Meridional integration of AAM gives global AAM (GAAM; Eq. (2)). On interannual or shorter time scales, changes in the solid Earth's angular momentum are mainly driven by atmospheric interactions[9]. Thus, assuming that the Earth's moment of inertia is nearly constant, the perturbation in LOD can be attributed to the perturbation in GAAM as shown in Eq. (3) and discussed in ref. 22. Unlike the ref. 22, we assume a shallow atmosphere, with constant radial distance from the Earth's core to all atmospheric levels. The shallow atmosphere assumption is applicable since nearly 99.9% of the atmospheric mass is located within the troposphere and stratosphere, or within ~50 km from the Earth's surface. Unless the zonal wind in the levels above is several orders of magnitude greater than that in the lower levels, the vast majority of the AAM would come from the lower atmosphere. For the troposphere and stratosphere, the percentage error in approximating the radius from the Earth's center to that at the surface is less than 1%. Thus, applying the shallow atmosphere assumption would not significantly change the AAM values while simplifying the calculation.

To compute AAM, we used the Japanese 55-year Reanalysis data (JRA-55[34]) from 1960 to 2019 (60 years). The zonal wind (U) from JRA-55 is available at 37 levels from 1000-hPa to 1-hPa levels at horizontal resolution of 1.25° in latitude and longitude. Monthly U is used in Eq. (1), but daily U gives almost identical results. We have also conducted the same analysis with the European Centre for Medium-Range Weather Forecasts Reanalysis version 5 (ERA5[35]) and found consistent results (compare Fig. 2 and Supplementary Fig. 2).

To ascertain the ability to predict LOD variability, a set of decadal hindcasts from the Coupled Model Intercomparison Project phase 6 (CMIP6) decadal climate prediction project (DCPP) is used[36]. The nine models used in this study are listed in Table 1. Each model is classified as high-top or low-top model by applying a 1-hPa criterion for the model top level[31], which results in six high-top models and three low-top models. Each model's hindcast is initialized every October or November from 1960 to 2016 (57 years) or every January from 1961 to 2017 (57 years). Similar to reanalysis, AAM and LOD are calculated using monthly U without any horizontal interpolation. Then, for multi-model mean (MMM), each model's ensemble mean forecast starting from the first January after initialization is interpolated to the coarsest horizontal model resolution available.

Tropical climate variability

For ENSO index, sea surface temperature (SST) anomaly in the Niño3 region (5°S–5°N, 150°W–90°W) is used. Although not shown, using 30-year moving climatology according to the NOAA CPC definition gives almost identical results. The SST data are obtained from the Extended Reconstructed Sea Surface Temperature version 5 (ERSSTv5) dataset[37] from 1960 to 2019 (60 years). For QBO index, the zonal-mean zonal wind anomaly at 30-hPa level averaged over 5°S–5°N from JRA-55 is used for the same analysis period. Here, the Niño region and QBO level are chosen as those that maximize the correlation of each index with LOD anomaly in observation (Supplementary Tables 3, 4).

To test whether LOD anomaly variation is associated with ENSO or QBO, the multiple linear regression of the observed LOD anomaly to lagged ENSO and QBO indices from observation is performed. The combination with the highest R^2, or that best explains the LOD anomaly variation, is chosen as the optimally reconstructed LOD index. Data from 1965 to 2016 (52 years) are used for regression, which is approximately the years with valid LOD anomaly after removing 5-year running mean. The optimal LOD index reconstructed with ENSO and QBO ($\mathrm{LOD_{E\&Q}}$ or ENSO&QBO-based index) and that with ENSO only ($\mathrm{LOD_E}$ or ENSO-based index) are:

$$\begin{aligned}\mathrm{LOD_{E\&Q}}(t) = {} & 1.0 \times 10^{-4} \times \mathrm{ENSO}(t-1) + 3.9 \times 10^{-6} \\ & \times\ \mathrm{QBO}(t-1) + 5.7 \times 10^{-6}\end{aligned} \tag{4}$$

$$\mathrm{LOD_E}(t) = 1.0 \times 10^{-4} \times \mathrm{ENSO}(t-1) + 5.1 \times 10^{-6} \tag{5}$$

When the reconstructed index is calculated with MMM prediction, the regression coefficients are similar to the above values. One subtle difference between MMM prediction and observation is that, while LOD anomaly lags one month behind ENSO and QBO in observations, they have a simultaneous relationship in MMM prediction. Further information of regression results for observation and MMM are provided in Supplementary Tables 5, 6.

Measure of prediction skill

The prediction skill is evaluated by using the anomaly correlation coefficient (ACC) which is defined as follows:

$$\mathrm{ACC}(t) = \frac{\frac{1}{n}\sum_{j=1}^{n}\left(O_{jt} - \bar{O}_t\right)\left(M_{jt} - \bar{M}_t\right)}{\sqrt{\frac{1}{n}\sum_{j=1}^{n}\left(O_{jt} - \bar{O}_t\right)^2}\sqrt{\frac{1}{n}\sum_{j=1}^{n}\left(M_{jt} - \bar{M}_t\right)^2}} \quad (6)$$

$$\bar{O}_t = \frac{1}{n}\sum_{j=1}^{n} O_{jt}, \bar{M}_t = \frac{1}{n}\sum_{j=1}^{n} M_{jt} \quad (7)$$

where O and M represent the observation (or reanalysis) and model prediction, respectively, and overbar indicates their climatological mean. Here, t is the forecast lead time ($t = 1, 2, \ldots, 37$ month), j is the initialization year, and n is the total number of initialization years ($n = 57$).

Statistical tests

Pearson's correlation is used as a measure of correlation. Standard deviation is provided as an indicator of variability. Adjusted Fisher-Pearson standardized moment coefficient is used to calculate sample skewness.

Two-tailed Student's t-test is used to judge whether regression or correlation coefficients are statistically significant at the 95% confidence level, assuming independent and identically distributed samples following normal distribution. Based on the identical assumption, a two-tailed F-test for equality of variances is conducted to determine whether AAM variabilities of reanalysis and MMM are significantly different at the 95% confidence level. A 95% confidence interval for the correlation coefficient is calculated using Fisher's Z-transformation, which also assumes independent and identically distributed samples. The 95% confidence intervals for standard deviation and skewness are estimated using chi-squared distribution and normal distribution, respectively, with the same assumption as the two-tailed Student's t-test.

Reporting summary

Further information on research design is available in the Nature Research Reporting Summary linked to this article.

Data availability

All data sets used in this study are publicly available. The EOP 14 C04 data is downloaded from https://www.iers.org/IERS/EN/DataProducts/EarthOrientationData/eop.html. A detailed explanation is provided at http://eoppcc.cbk.waw.pl/. The ERSSTv5 data[37] is freely available at https://www.ncei.noaa.gov/products/extended-reconstructed-sst. The JRA-55 reanalysis data[34] is freely available at https://doi.org/10.5065/D60G3H5B. CMIP6 model outputs can be obtained from https://pcmdi.llnl.gov/CMIP6/.

Code availability

The code to calculate AAM was built upon the code written by ref. [22] available at https://zenodo.org/records/7003975. All codes for the analyses in this paper are available from the first author (yhs11088@snu.ac.kr) upon reasonable request.

Received: 16 December 2023; Accepted: 4 March 2024;
Published online: 14 March 2024

References

1. Hide, R. & Dickey, J. O. Earth's variable rotation. *Science* **253**, 629–637 (1991).
2. Stephenson, F. R. & Morrison, L. V. Long-term changes in the rotation of the Earth: 700 B.C. to A.D. 1980. *Philos. Trans. R. Soc. Lond. Ser. A* **313**, 47–70 (1984).
3. Morrison, L. V. & Stephenson, F. R. Historical eclipses and the variability of the Earth's rotation. *J. Geodyn.* **32**, 247–265 (2001).
4. Eubanks, T. M. Variations in the orientation of the Earth. In: *Contributions of Space Geodesy to Geodynamics: Earth Dynamics* (eds Smith, D. E. & Turcotte, D. L.) 1–54 (American Geophysical Union, 1993).
5. Jault, D., Gire, C. & Le Mouël, J. L. Westward drift, core motions and exchanges of angular momentum between core and mantle. *Nature* **333**, 353–356 (1988).
6. Mound, J. E. & Buffett, B. A. Interannual oscillations in length of day: implications for the structure of the mantle and core. *J. Geophys. Res.* **108**, 2334 (2003).
7. Rosen, R. D. The axial momentum balance of Earth and its fluid envelope. *Surv. Geophys.* **14**, 1–29 (1993).
8. Weickmann, K. M., Kiladis, G. N. & Sardeshmukh, P. D. The dynamics of intraseasonal atmospheric angular momentum oscillations. *J. Atmos. Sci.* **54**, 1445–1461 (1997).
9. Gross, R. S., Fukumori, I., Menemenlis, D. & Gegout, P. Atmospheric and oceanic excitation of length-of-day variations during 1980–2000. *J. Geophys. Res.* **109**, B01406 (2004).
10. Le Bail, K., Gipson, J. M. & MacMillan, D. S. Quantifying the correlation between the MEI and LOD variations by decomposing LOD with singular spectrum analysis. In: *Earth on the Edge: Science for a Sustainable Planet* (eds. Rizos, C. & Willis, P.) 473–477 (Springer, 2014).
11. Gipson, J. El Niño and VLBI measured length of day. In: *IVS 2016 General Meeting Proceedings: New Horizons with VGOS* (eds Behrend, D. et al.) 336–340 (2016).
12. Chao, B. F. Interannual length-of-day variation with relation to the Southern Oscillation/El Nino. *Geophys. Res. Lett.* **11**, 541–544 (1984).
13. Chao, B. F. Length-of-day variations caused by El Niño–Southern Oscillation and Quasi-Biennial Oscillation. *Science* **243**, 923–925 (1989).
14. Dickey, J. O., Marcus, S. L., Eubanks, T. M. & Hide, R. Climate studies via space geodesy: Relationships between ENSO and interannual length-of-day variation. In: *Interactions Between Global Climate Subsystems: The Legacy of Hann* (eds. McBean, G. A. & Hantel, M.) 141–155 (Americal Geophysical Union, 1993).
15. Dickey, J. O., Marcus, S. L. & Chin, T. M. Thermal wind forcing and atmospheric angular momentum: Origin of the Earth's delayed response to ENSO. *Geophys. Res. Lett.* **34**, L17803 (2007).
16. Raut, S., et al. Investigating the relationship between length of day and El-Niño using wavelet coherence method. In: *Geodesy for a Sustainable Earth* (eds Freymueller, J. T. & Sánchez, L.) 253–258 (Springer, 2022).
17. Reid, G. C. & Gage, K. S. A relationship between the height of the tropical tropopause and the global angular momentum of the atmosphere. *Geophys. Res. Lett.* **11**, 840–842 (1984).
18. Gross, R. S., Marcus, S. L., Eubanks, T. M., Dickey, J. O. & Keppenne, C. L. Detection of an ENSO signal in seasonal length-of-day variations. *Geophys. Res. Lett.* **23**, 3373–3376 (1996).
19. Mo, K. C., Dickey, J. O. & Marcus, S. L. Interannual fluctuations in atmospheric angular momentum simulated by the National Centers for Environmental Prediction medium range forecast model. *J. Geophys. Res.* **102**, 6703–6713 (1997).
20. Weickmann, K., Berry, E., Gensini, V., Gold, D. & Petroski, T. Changes in the global climate: atmospheric angular momentum and Pacific ocean temperatures. *J. Clim.* **36**, 6597–6611 (2023).
21. Le Mouël, J. L., Lopes, F., Courtillot, V. & Gibert, D. On forcings of length of day changes: from 9-day to 18.6-year oscillations. *Phys. Earth Planet. Inter.* **292**, 1–11 (2019).
22. Scaife, A. A. et al. Long-range predictability of extratropical climate and the length of day. *Nat. Geosci.* **15**, 789–793 (2022).
23. Hendon, H. H. Length of day changes associated with the Madden-Julian Oscillation. *J. Atmos. Sci.* **52**, 2373–2383 (1995).
24. Feldstein, S. B. An observational study of the intraseasonal poleward propagation of zonal mean flow anomalies. *J. Atmos. Sci.* **55**, 2516–2529 (1998).

25. James, I. N. & Dodd, J. P. A mechanism for the low-frequency variability of the mid-latitude troposphere. *Q. J. R. Meteorol. Soc.* **122**, 1197–1210 (1996).
26. Lee, S., Son, S.-W., Grise, K. & Feldstein, S. B. A mechanism for the poleward propagation of zonal mean flow anomalies. *J. Atmos. Sci.* **64**, 849–868 (2007).
27. Choi, J. & Son, S.-W. Seasonal-to-decadal prediction of El Niño–Southern Oscillation and Pacific Decadal Oscillation. *NPJ Clim. Atmos. Sci.* **5**, 29 (2022).
28. Wilks, D. S. *Statistical Methods in the Atmospheric Sciences* (Elsevier, 2019).
29. Scaife, A. A. et al. Predictability of the quasi-biennial oscillation and its northern winter teleconnection on seasonal to decadal timescales. *Geophys. Res. Lett.* **41**, 1752–1758 (2014).
30. Pohlmann, H. et al. Improved forecast skill in the tropics in the new MiKlip decadal climate predictions. *Geophys. Res. Lett.* **40**, 5798–5802 (2013).
31. Charlton-Perez, A. J. et al. On the lack of stratospheric dynamical variability in low-top versions of the CMIP5 models. *J. Geophys. Res. Atmos.* **118**, 2494–2505 (2013).
32. Baldwin, M. P. et al. The quasi-biennial oscillation. *Rev. Geophys.* **39**, 179–229 (2001).
33. Gabis, I. P. Seasonal dependence of the quasi-biennial oscillation (QBO): New evidence from IGRA data. *J. Atmos. Sol. Terr. Phys.* **179**, 316–336 (2018).
34. Kobayashi, S. et al. The JRA-55 reanalysis: general specifications and basic characteristics. *J. Meteorol. Soc. Jpn. Ser. II* **93**, 5–48 (2015).
35. Hersbach, H. et al. The ERA5 global reanalysis. *Q. J. R. Meteorol. Soc.* **146**, 1999–2049 (2020).
36. Boer, G. J. et al. The Decadal Climate Prediction Project (DCPP) contribution to CMIP6. *Geosci. Model Dev.* **9**, 3751–3777 (2016).
37. Huang, B. et al. Extended Reconstructed Sea Surface Temperature, version 5 (ERSSTv5): upgrades, validations, and intercomparisons. *J. Clim.* **30**, 8179–8205 (2017).

Acknowledgements

This research was supported by the Korea Meteorological Administration Research and Development Program under Grant KMI2022-01114 and Basic Science Research Program through the National Research Foundation of Korea (NRF) funded by the Ministry of Education (NRF-2022R1I1A1A01064026). A.A.S. was supported by the Met Office Hadley Centre Climate Programme (HCCP) funded by BEIS and Defra.

Author contributions

H.Y. carried out the analysis of the data. J.C. provided detailed guidelines about the analysis method and contributed to the interpretation of the results. S.-W.S. outlined the research, guided the direction of analysis, and arranged the main figure set. A.A.S. gave helpful feedback and comments on the manuscript. All helped to write the manuscript.

Competing interests

The authors declare no competing interests.

Additional information

Supplementary information The online version contains

supplementary material available at https://doi.org/10.1038/s41612-024-00616-2.

Correspondence and requests for materials should be addressed to Jung Choi or Seok-Woo Son.